Interferometric Synthetic Aperture Microwave Radiometry for the Remote Sensing of the Earth

CHRISTOPHER S. RUF, MEMBER, IEEE, CALVIN T. SWIFT, FELLOW, IEEE, ALAN B. TANNER, AND DAVID M. LE VINE, SENIOR MEMBER, IEEE

Abstract—**Interferometric aperture synthesis is presented as an alternative to real aperture mesurements of the earth's brightness temperature from low earth orbit. Real apertures become impractically large as the spatial resolution requirements from space at microwave frequencies increase. Image synthesis techniques developed for radio astronomy that utilize the interference pattern formed by cross-correlating a pair of spatially separated antenna elements offer an attractive alternative to the real aperture. Fundamental differences in the requirements of an earth viewing microwave sensor from those of a radio telescope present new engineering challenges when using the techniques of radio astronomy in a geoscience application. In particular, the brightness temperature distribution of an earth remote sensor typically fills the entire field of view of the individual antenna elements, whereas the flux density incident on a radio telescope antenna often originates from a relatively small percentage of the antenna mainbeam. The relationship between the brightness temperature distribution under observation and the noise floor on the image of that distribution which results from interferometric aperture synthesis is developed. Resulting antenna design considerations concerning the appropriate configuration of antenna elements in an interferometric array are derived. A preliminary design and performance characterization of a 1.4-GHz interferometric radiometer that is presently under construction is also presented.**

INTRODUCTION

PASSIVE microwave remote sensing of the earth's surface has progressed considerably in recent years. Surface parameters of fundamental geophysical interest have been detected and monitored by airborne and spaceborne microwave radiometers. These parameters include sea surface temperature [1], salinity [2] and windspeed [3], soil moisture content [4], and arctic sea ice concentration [5]. The spatial resolution of these measurements from low earth orbit has been constrained by the antenna aperture size available on orbiting platforms. For example, a 1-m aperture allows for approximately 15–150 km spatial resolution over the frequency range 20–2 GHz, respectively. User requirements for resolution on the order of 1 km at these frequencies will require much larger antennas.

Current plans for the earth observing system (EOS) polar-orbiting space platform allow for the development of large space structures, including antennas, in low earth orbit. Large antennas will guarantee the desired spatial resolution. However, scanning of the narrow antenna beam is a potential problem. Smaller microwave radiometers are typically scanned mechanically; this technique becomes impractical with very large antennas. Furthermore, the dwell time available on each pixel of a high-resolution pencil beam scanning imager is in many applications insufficient to produce satisfactory data. One solution to the scanning problem is the generation of simultaneous pencil beams aligned crosstrack to the direction of motion of the sensor.

Simultaneous pencil beams can be generated by an antenna system in a variety of ways. The push broom radiometer provides the necessary antenna pattern with a parallel bank of radiometers [6], [7]. The radiometers are connected to a line of antenna feeds that share a single reflecting dish. The size and tolerance requirements of such a dish—100 m diameter for 1-km resolution at 3 GHz—are at present prohibitive for spaceborne applications.

An alternative to this "brute force" method of imaging is the phased array. Coherent addition of the fields excited at a distribution of small array elements provides the spatial resolution of a large dish in a manner more suitable to the space platform. Individual elements can be manufactured on earth and simply deployed in their array configuration. A filled array, in which the antenna elements are distributed uniformly over a lattice, reduces the tolerance requirements of the reflecting dish but not the size. A thinned array, however, reduces both. Thinned array passive microwave remote sensing has found widespread applications in radio astronomy under the name of synthetic aperture interferometry [8], [9]. The adaptation of the engineering principles and technology developed by radio astronomy to earth remote sensing is the subject of this paper.

The paper is divided into six parts. Part I begins with a

Manuscript received October 2, 1987; revised March 18, 1988.

C. S. Ruf was with the Microwave Remote Sensing Laboratory, University of Massachusetts, Amherst. He is now with the Microwave Advanced Systems Group, Jet Propulsion Laboratory, California Institute of Technology, Pasadena, CA 91109.

C. T. Swift, and A. B. Tanner are with the Microwave Remote Sensing Laboratory, University of Massachusetts, Amherst, MA 01003.

D. M. Le Vine, Microwave Sensors Branch, Goddard Laboratory for Atmospheric Science, NASA Goddard Space Flight Center Greenbelt, MD 20771.

IEEE Log Number 8821766.

review of the imaging fundamentals of interferometric aperture synthesis. It will serve more to establish the nomenclature to be used later in the paper than as a complete formulation of the topic. Part II characterizes the signal-to-noise performance of a single interferometric measurement. This characterization will be used as a building block for the analysis of various complete imaging systems. Part III addresses the noise characteristics of the brightness temperature image produced from the interferometer measurements. The sampling requirements of the measurements, the image reconstruction procedure applied to the measurements, and the resulting effects of the noise in the measurements on the image are described. Part IV applies the results of the previous sections to a specific example, the electronically steered thinned array radiometer (ESTAR)[1] currently under construction by the authors. The ESTAR prototype is described in detail sufficient to permit a performance evaluation of its spatial and temperature resolution. Part V assesses critical aspects of an extension of the ESTAR sensor to a larger spaceborne system. Of particular importance are the number and placement of antenna elements in the imaging array. Part VI concludes with a comparison of the implementation methodologies of radio astronomy and earth remote sensing. The effects of the source brightness distribution, the antenna array configuration, and the method used for array scanning are discussed.

I. Interferometric Imaging Fundamentals

An imaging radiometer maps the brightness temperature distribution over a given field of view (FOV). Real aperture radiometers do this by scanning their antenna—either mechanically or electrically—across the FOV. The resolution of the image is consequently determined by the beamwidth of the antenna. Interferometric imaging radiometers, on the other hand, generate an image indirectly, by measuring the Fourier transform of the brightness temperature distribution over the FOV. This measurement, which is referred to as the visibility function by radio astronomers, is inverse Fourier transformed by the user to form an image.

Interferometer measurements are made by cross-correlating the RF signals received by two spatially separated antennas that have an overlapping FOV. An example of such a measurement system is illustrated in Fig. 1. A pair of antenna elements is deployed at a height h above the surface of the earth. Their antenna patterns are coincident and constitute the FOV of the eventual image. A coordinate system is centered at one of the antennas such that the surface of the earth (flat approximation) lies on the $z = h$ plane. The second antenna is located at coordinates $(x, y, z) = (D_x, D_y, 0)$.

The thermal emission by the earth provides an incident flux density $S_{\text{inc}}((x, y), f, (\theta, \phi))$ at the antennas, where (x, y) is the antenna location in the XY plane, f is the frequency of the emission, and (θ, ϕ) is the solid angle locating the incoming direction of the emission. S_{inc} is measured in units of W/m^2 − Hz − sr. If the antennas had isotropic antenna patterns, the power available at their output terminals per unit steradian would be

$$P_{\text{inc}}(\theta, \phi) = \tfrac{1}{2} S_{\text{inc}}(\theta, \phi) A_{\text{iso}} B \qquad (1)$$

where

- P_{inc} is in units of W/sr
- $\frac{1}{2}$ accounts for the polarization of the antennas
- $A_{\text{iso}} = \lambda^2/4\pi$ is the effective aperture of an isotropic antenna (in m^2)
- B is the bandwidth of the signal (in Hz).

The subscript "inc" assigned to $P(\theta, \phi)$ refers to the fact that all incident radiation is received equally by an isotropic antenna. The corresponding incident brightness temperature per steradian $T_{\Omega_{\text{inc}}}(\theta, \phi)$ is defined by

$$T_{\Omega_{\text{inc}}}(\theta, \phi) = \frac{1}{kB} P_{\text{inc}}(\theta, \phi) \qquad (2)$$

where k is Boltzmann's constant.

The actual received brightness temperature per steradian $T_\Omega(\theta, \phi)$ includes the gain effects of the actual, non-isotropic, antenna pattern

$$T_\Omega(\theta, \phi) = T_{\Omega_{\text{inc}}}(\theta, \phi)\, G(\theta, \phi) \qquad (3)$$

where $G(\theta, \phi)$ is the directive gain pattern of the antennas. The measured brightness temperature T_B follows from

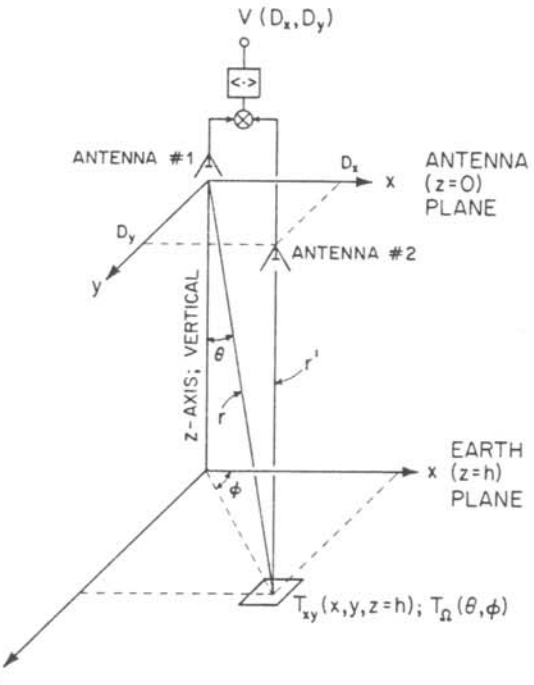

Fig. 1. A two-dimensional earth viewing interferometer—The two antennas in the $z = 0$ plane have antenna patterns directed toward the earth ($z = h$ plane). The cross-correlation of the RF outputs from the two antennas produces a sample of the visibility function, $V(D_x, D_y)$, determined by the relative antenna spacing. The visibility function is the two-dimensional Fourier transform of the brightness temperature distribution on the earth $T_{XY}(x/h, y/h)$.

[1]This acronym was coined by F. T. Barath of the Jet Propulsion Laboratory.

(3) by integrating over all solid angles

$$T_B = \int_0^{2\pi} \int_0^{\pi} T_\Omega(\theta, \phi) \sin\theta \, d\theta \, d\phi. \quad (4)$$

Equations (1)–(4) define a variable $T_\Omega(\theta, \phi)$ in units of K/sr, which is not a part of the standard earth remote-sensing nomenclature. It serves to make the connection between the language of astronomy and geoscience. It is also a useful part of the mathematics of synthetic aperture imaging of a brightness temperature distribution. Note that, while T_B is directly measurable, $T_\Omega(\theta, \phi)$ is a mathematical construct only. It is formed by dividing T_B by the appropriate solid angle. For example, consider the case of an antenna that is completely enclosed in a black body at a physical temperature of T_0 K. The incident brightness temperature distribution per steradian is immediately given by

$$T_{\Omega_{\text{inc}}}(\theta, \phi) = \frac{T_0}{4\pi}. \quad (5)$$

The measured brightness temperature is then

$$T_B = \frac{T_0}{4\pi} \int_0^{2\pi} \int_0^{\pi} G(\theta, \phi) \sin\theta \, d\theta \, d\phi$$
$$= T_0 \quad (6)$$

where $\int_0^{2\pi} \int_0^{\pi} G(\theta, \phi) \sin\theta \, d\theta \, d\phi = 4\pi sr$ by definition. Referring back to Fig. 1, a cross-correlation of the signals produced by a separated pair of similar antennas viewing the same brightness temperature distribution $T_\Omega(\theta, \phi)$ produces a sample of the visibility function given by

$$V(u, v) = \int_0^{2\pi} \int_0^{\pi} T_\Omega(\theta, \phi) \cdot e^{j2\pi(u\sin\theta\cos\phi + v\sin\theta\sin\phi)} \sin\theta \, d\theta \, d\phi \quad (7)$$

where

V is in units of K
$u = D_x/\lambda$, $v = D_y/\lambda$
D_x and D_y are the relative antenna spacings (see Fig. 1)
λ is the wavelength of the incident radiation at the antennas.

Equation (7) is a restatement of a relationship that is central to interferometric radio astronomy [9]. It is also derived in Appendix I of this paper from an earth viewing perspective, as mathematical preparation for the signal-to-noise analysis of Part II.

The brightness temperature image $\hat{T}_B(\theta, \phi)$ is formed by an inverse Fourier transformation of the measurements

$$\hat{T}_B(\theta, \phi) = \int_{-\infty}^{\infty} \int_{-\infty}^{\infty} V(u, v) \cdot e^{-j2\pi(u\sin\theta\cos\phi + v\sin\theta\sin\phi)} \, du \, dv. \quad (8)$$

II. Correlator Signal-To-Noise Characterization

All microwave radiometer measurements have associated with them an inherent noise floor, or "ΔT", due to the finite integration time available for the measurement. The ΔT of a radiometer represents the standard deviation in the estimated brightness temperature, expressed in Kelvins. For a real aperture total power radiometer, this noise floor is given by [10]

$$\Delta T = \frac{T_B + T_R}{\sqrt{B\tau}} \quad (9)$$

where

T_B is the brightness temperature of the scene (in K)
T_R is the effective receiver noise temperature (in K)
B is the pre-detection bandwidth (in Hz)
τ is the integration time (in S).

Other sources of error in a radiometer measurement (e.g., calibration, drifts, biases) can in principle be made arbitrarily small by careful engineering. The ΔT noise floor, however, is unavoidable. Modern state-of-the-art radiometer systems routinely operate very near this performance limit. In situations in which the integration time available for each measurement is severely constrained—notably, earth remote sensing from low earth orbit with a narrow FOV in the direction of satellite motion—the ΔT of a radiometer often determines its effectiveness.

The ΔT of the brightness temperature image produced by interferometric aperture synthesis is a fundamental performance characteristic of the imager. This noise floor can be derived by first considering the standard deviation in the individual samples of the visibility function from which the image is constructed. This formulation will then serve as a building block for determining the ΔT of various specific implementations of the synthetic aperture interferometer.

The visibility function is sampled by cross-correlating the signals from two antennas. A hardware schematic of the correlator is shown in Fig. 2. Referring to the figure, the time varying processes entering the two antennas are given by (AI.7) and (AI.8). The RF bandpass characteristics of the hardware, labelled "BPF" in the figure, have been incorporated into the power spectral density of the processes. Additive Gaussian receiver noise in the two channels of the correlator can likewise be represented by equivalent noise processes $n_1(t)$ and $n_2(t)$ at the antennas. The power spectral density of this noise is given by

$$S_{n_i}(f) = \frac{1}{2B} T_{R_i} \quad \text{for } f_c - \frac{B}{2} < |f| < f_c + \frac{B}{2}$$
$$= 0 \quad \text{otherwise} \quad (10)$$

where

S_n is in units of K/Hz
$i = 1, 2$ designates the antenna channel
T_{R_i} is the receiver noise temperature of the ith channel.

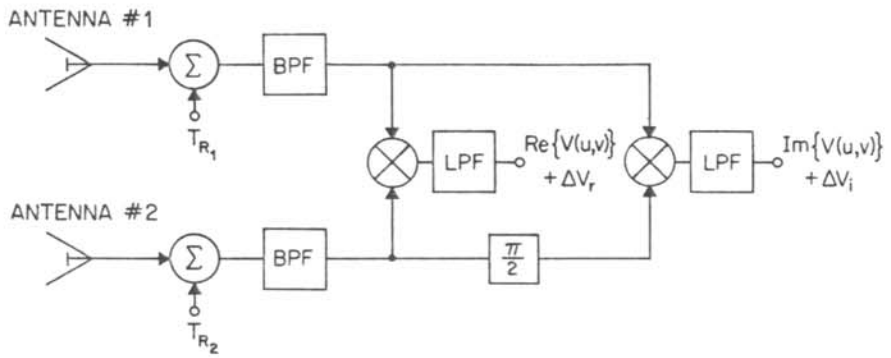

Fig. 2. Quadrature (complex) antenna correlator—Receiver noise is added at the antenna terminals. The signals are bandpass filtered prior to quadrature correlation. The finite duration time integration is represented as a lowpass filter. The output real and imaginary components of the visibility function are corrupted by statistically dependent additive noise with standard deviations ΔV_r and ΔV_i, respectively.

The signals in the two channels are cross-correlated in phase quadrature. This amounts to one direct multiplication of the two signals producing the in-phase, or real, component of the cross-correlation, and one multiplication of the signal in one channel with a 90° phase shifted version of the signal in the other channel producing the quadrature, or imaginary, component. These multiplications are performed in parallel and are each followed by an integrator. The integration is modeled by the following lowpass filter transfer function:

$$H_{LP}(f) = 1, \quad \text{for } |f| < \frac{1}{2\tau}$$
$$= 0, \quad \text{otherwise} \tag{11}$$

where

τ is the equivalent integration time (in seconds) appropriate for this model of the integrator.

The output of the integrators is a noisy sample of the real and imaginary components of the visibility function. The standard deviations in the visibility samples $\Delta V_{r,i}$ are derived in Appendix II as

$$\Delta V_r(u, v) = \left(\frac{1}{2B\tau}\right)^{1/2} [(T_B + T_{R_1})(T_B + T_{R_2}) + V_r^2(u, v) - V_i^2(u, v)]^{1/2} \tag{12}$$

$$\Delta V_i(u, v) = \left(\frac{1}{2B\tau}\right)^{1/2} [(T_B + T_{R_1})(T_B + T_{R_2}) + V_i^2(u, v) - V_r^2(u, v)]^{1/2} \tag{13}$$

where

ΔV_r is the standard deviation in the real component of $V(u, v)$ (in units of K)

ΔV_i is the standard deviation in the imaginary component of $V(u, v)$ (in units of K)

T_B is given by (4)

$V_r(u, v) = \int_0^{2\pi} \int_0^{\pi} T_\Omega(\theta, \phi) \cos [2\pi(u \sin\theta \cos\phi + v \sin\theta \sin\phi)] \sin\theta \, d\theta \, d\phi$

$V_i(u, v) = \int_0^{2\pi} \int_0^{\pi} T_\Omega(\theta, \phi) \sin [2\pi(u \sin\theta \cos\phi + v \sin\theta \sin\phi)] \sin\theta \, d\theta \, d\phi$

Equations (12) and (13) are general, scene dependent, expressions for the noise inherent in an interferometer measurement. Only special cases of these relationships have previously appeared in the literature. For example, the standard expression for the "ΔV" in radio astronomy applications is found by letting $u = v = 0$ [17]. The "ΔT" for a total power radiometer, given by (9), results from the special case $u = v = 0$, $T_{R_1} = T_{R_2}$, and $\Delta T = (\Delta V_r^2 + \Delta V_i^2)^{1/2}$, corresponding to a square-law detector viewed as the modulus of a complex correlator. Note, finally, that the total integrated brightness temperature across the FOV, T_B, contributes to the noise floor of every sample of the visibility function. This noise will be shown to accumulate adversely in the image reconstruction process.

III. Image Reconstruction and Sensitivity

The image reconstruction formula described by (8) requires that the visibility function be sampled at all possible relative antenna positions (u, v). In practice, samples are taken up to some maximum antenna spacing due to the size constraints on the sensor. In addition, the finite extent of the brightness temperature distribution defined by the antenna patterns (FOV) allows the (u, v) samples to be taken at discrete steps without loss of information, as provided by the Nyquist sampling theorem in two dimensions. These discrete samples can then be combined in a truncated discrete approximation to the integral Fourier transform given by (8) to reconstruct an estimate of the brightness temperature distribution.

The sampling requirements are satisfied by visibility measurements made over a lattice

$$D_{x_i} = i\frac{\lambda}{2}, \quad u_i = \frac{i}{2}; \qquad i = 0, \pm 1, \pm 2, \cdots, \pm N_x$$
$$D_{y_k} = k\frac{\lambda}{2}, \quad v_k = \frac{k}{2}: \qquad k = 0, \pm 1, \pm 2, \cdots, \pm N_y. \tag{14}$$

This places the aliased responses in the image (grating lobes in the synthesized antenna pattern) outside of the FOV in all cases. (In cases where the FOV is significantly

smaller than the complete halfspace $\theta < \pi/2$ and $|\phi| < \pi$, the antenna elements may be spread out at greater than $\lambda/2$ intervals.) The corresponding image reconstruction formula is

$$\hat{T}_B(\theta, \phi) = \sum_{i=-N_x}^{N_x} \sum_{k=-N_y}^{N_y} V(u_i, v_k) e^{-j2\pi(u_i \sin\theta\cos\phi + v_k \sin\theta\sin\phi)} \tag{15}$$

where $\hat{T}_B(\theta, \phi)$ is the estimate of the brightness temperature distribution at (θ, ϕ). In practice, (15) will be modified by a transform window taper to reduce the sidelobes of the synthesized antenna pattern.

The spatial resolution of the image follows by expanding (15) using (7):

$$\hat{T}_B(\theta, \phi) = \int_0^{2\pi} \int_0^{\pi} T_\Omega(\theta', \phi')\, AF_x(\theta, \theta'; \phi, \phi') \cdot AF_y(\theta, \theta'; \phi, \phi') \sin\theta'\, d\theta'\, d\phi' \tag{16}$$

where

$$AF_x(\theta, \theta'; \phi, \phi') = \frac{\sin\left[\pi \frac{2N_x + 1}{2} (\sin\theta\cos\phi - \sin\theta'\cos\phi')\right]}{\sin\left[\frac{\pi}{2} (\sin\theta\cos\phi - \sin\theta'\cos\phi')\right]}$$

$$AF_y(\theta, \theta'; \phi, \phi') = \frac{\sin\left[\pi \frac{2N_y + 1}{2} (\sin\theta\sin\phi - \sin\theta'\sin\phi')\right]}{\sin\left[\frac{\pi}{2} (\sin\theta\sin\phi - \sin\theta'\sin\phi')\right]}.$$

$AF_{x,y}$ corresponds to the array factor used in standard phased array terminology. For example, the spatial resolution along the x-axis directly beneath the antennas ($\theta = 0$, $\phi' = 0$) is defined as the angular distance between the first zeros of AF_x

$$\Delta\theta_x = \sin^{-1}\left(\frac{4}{2N_x + 1}\right). \tag{17}$$

Similarly, the spatial resolution in y at $\theta = 0$ is given by

$$\Delta\theta_y = \sin^{-1}\left(\frac{4}{2N_y + 1}\right). \tag{18}$$

For sufficiently high resolution cases ($N_{x,y} >> 1$, $\Delta\theta \approx \sin\Delta\theta$), the angular resolution becomes

$$\Delta\theta_{x,y} = \frac{2\lambda}{D_{x,y_{\max}}} \text{ rad} \tag{19}$$

where $D_{x,y_{\max}}$ are the maximum antenna spacings in the x and y directions on the uv-plane. This null-to-null resolution corresponds exactly with the spatial resolution of a real aperture antenna of size D_x-by-D_y with a uniform amplitude taper over the aperture. The transform window taper mentioned above will degrade the spatial resolution of the image in the same way as does the amplitude taper on a real aperture. There is, however, one important difference between this synthesized array factor and its real aperture or phased array analogues. A uniform transform window taper here will produce 6.6-dB sidelobe levels instead of the 13-dB sidelobes normally associated with a uniform taper. This is because the visibility function is a power, not a voltage, measurement. The 13-dB first sidelobe level can be recovered by a triangular transform window taper, which is the self-convolution of a uniform taper and, therefore, effectively squares the resulting array factors. Any additional sidelobe suppression could be achieved by adding a second taper. It is interesting to note that, in practice, only half of the uv-plane need be measured directly since the visibility function has Hermitian symmetry ($V(u, v) = V^*(-u, -v)$). This implies that the actual physical aperture required to produce an image with the resolution described by (19) is only $\frac{1}{2} D_{x,y_{\max}}$. This factor of two apparent savings in aperture (or increase in resolution) is exactly cancelled out by the triangular taper needed to synthesize a conventional uniform voltage distribution. This taper will both reduce the sidelobe level by a factor of two (in dB) and double the null-to-null resolution.

The visibility samples used in the image reconstruction formula given by (15) are actually time varying random processes, with statistics described in Appendix II. The resulting estimate of the brightness temperature distribution $\hat{T}_B(\theta, \phi)$ is, then, also corrupted by noise. The ΔT noise floor of this estimate is found from its power spectral density in the same way as was the standard deviation in the visibility samples. A general expression for this ΔT is rather complicated because of the statistical dependence of the noise in the individual visibility measurements on the measurements themselves, as expressed in (12) and (13). The image ΔT in one special case will help to illuminate the way in which measurement noise propagates through the image reconstruction to produce image noise.

If the nadir-looking image pixel is reconstructed, then the reconstruction formula (15) becomes

$$\hat{T}_B(\theta = 0) = \sum_{i=-N_x}^{N_x} \sum_{k=-N_y}^{N_y} V_r(u_i, v_k). \tag{20}$$

If, in addition, the brightness temperature distribution $T_\Omega(\theta, \phi)$ is assumed to be constant at all solid angles, then

$$V(u_i, v_k) = T_0 \quad \text{for } i = k = 0$$
$$= 0 \quad \text{otherwise} \tag{21}$$

where

T_0 is the constant brightness temperature (in K).

Under these conditions, the standard deviation (ΔT) in $\hat{T}_B$ given the noise floor (ΔV) in the measurements is

$$\Delta T = \left[\frac{(T_0 + T_{R_1})(T_0 + T_{R_2})}{B\tau} \frac{(2N_x + 1)(2N_y + 1)}{2} \right]^{1/2}. \tag{22}$$

Comparing (12) and (22), the standard deviation in the noise floor of the image has been increased by the root-sum-square of the noise in the individual measurements. This sum is over the terms in the image reconstruction formula. Note in particular that, because the noise in each visibility measurement is dependent on the total brightness temperature T_0 across the FOV, the noise in the final brightness temperature estimate at a particular point $\hat{T}_B(\theta, \phi)$ is dependent on all other points in the FOV. This distinction is generally not significant in radio astronomy applications, for which either the brightness temperature of the entire FOV is dominated by small, localized regions, is much smaller than the receiver noise, or both. For these reasons, sensitivity relationships used in radio astronomy often resemble (22) except that T_0 is interpreted as the brightness temperature not of the entire FOV, but rather of the particular region being imaged.

Comparing (9) and (22), the temperature resolution provided by a (real aperture) total power radiometer appears to have been degraded by a factor of the number of resolvable pixels. Again, this is a result of the dependence of each visibility measurement on the entire FOV, which is that same factor brighter than an individual pixel in this case. However, if the total power radiometer was required to produce a similar image in the same time (τ), the reduction in its available dwell time per pixel would exactly offset its apparent advantage.

IV. The Electronically Steered Thinned Array Radiometer (ESTAR)

The authors are currently constructing an interferometric synthetic aperture microwave radiometer, ESTAR. The sensor is being designed as a proof-of-concept and feasibility study for the application of passive aperture synthesis techniques to the remote sensing of the earth from low earth orbit. ESTAR operates at L-Band (1.4 GHz), for applications in the remote sensing of soil moisture content and sea surface salinity. The low operating frequency required for these measurements, combined with a desired spatial resolution of 1 to 10 km from low earth orbit, strongly suggests some form of synthetic aperture imaging. A one-dimensional analogue to the synthesis technique described above was chosen because of the along-track scanning automatically provided by an orbiting platform.

The ESTAR prototype currently under construction consists of five antenna elements and a bank of ten correlators that cross-correlate all possible pairs of antennas. The antennas are deployed along a line and are spaced at certain integer multiples of half the RF wavelengths so that the set of all cross-correlations will generate every half-wavelength spacing up to the maximum spacing while sampling each one as few times as possible. Such a configuration is known as a minimum redundancy linear array [11]. These optimally thinned arrays sample the visibility function (uv-plane) along a line at the appropriate Nyquist rate, with as few "redundancies" (duplicate samples) as possible. Redundant samples do not improve the spatial resolution of the resulting image. However, they have an important effect on the ΔT of the image. This section presents pertinent aspects of the ESTAR design, then proceeds to develop a working design equation for the determination of an optimum antenna array configuration. This relationship (46) explicitly states the effect that redundancies have on the ΔT of the image.

A schematic of the ESTAR prototype is diagrammed in Fig. 3. The coordinate system used has been modified from that of Fig. 1 in order to emphasize the one-dimensional nature of the imaging. The identical antenna elements are deployed over the $x = 0$ plane at a height h above the ground. Each individual antenna pattern is a fan beam directed toward the ground. Their directive gain patterns can be approximated by

$$\begin{aligned} G(\theta, \phi) &= G_0 \quad \text{for } \left|\frac{\pi}{2} - \theta\right| < \Delta\theta, \ |\phi| < \frac{\pi}{2} \\ &= 0 \quad \text{otherwise.} \end{aligned} \tag{23}$$

This corresponds to a FOV that is a strip across the earth ($x = h$ plane) along the y-axis, of width $\approx h\Delta\theta$. Imaging in the z-direction is provided by the forward motion of the sensor, which is also z-directed. This sweeps the FOV across the earth plane. In the y-direction, images are derived by interferometric aperture synthesis.

The y-component of the locations of the antenna elements in the antenna ($x = 0$) plane determines the sampling of the one-dimensional visibility function. For the particular array configuration shown in Fig. 3, antennas are located at $D_y = -2\lambda, -\lambda, 0, 1.5\lambda$, and 2λ. This results in relative antenna-pair spacings of $0.5\lambda, \lambda, \cdots, 4\lambda$ with redundant spacings at λ and 2λ. (Note that the "zeroeth" spacing required for the Fourier transformation of the visibility function is provided by self-correlating each of the individual elements.)

In general, the sampling performance of any thinned array can be summarized by its redundancies in the following manner: Let $N(\lambda/2)$ be the maximum relative antenna-pair spacing in a linear array for which all relative spacings from $0(\lambda/2)$ up to $N(\lambda/2)$ are present. Let r_n be the number of times that a relative spacing of $n(\lambda/2)$ is present in the array. Then the set $\{r_n\}_{n=0}^{N}$ determines the sampling performance of the thinned array. For example, the redundancy set for the ESTAR prototype described above is given by

$$\begin{aligned} r_n &= 1 \quad \text{for } n = 1, 3, 5, 6, 7, 8 \\ r_n &= 2 \quad \text{for } n = 2, 4 \\ r_n &= 5 \quad \text{for } n = 0. \end{aligned} \tag{24}$$

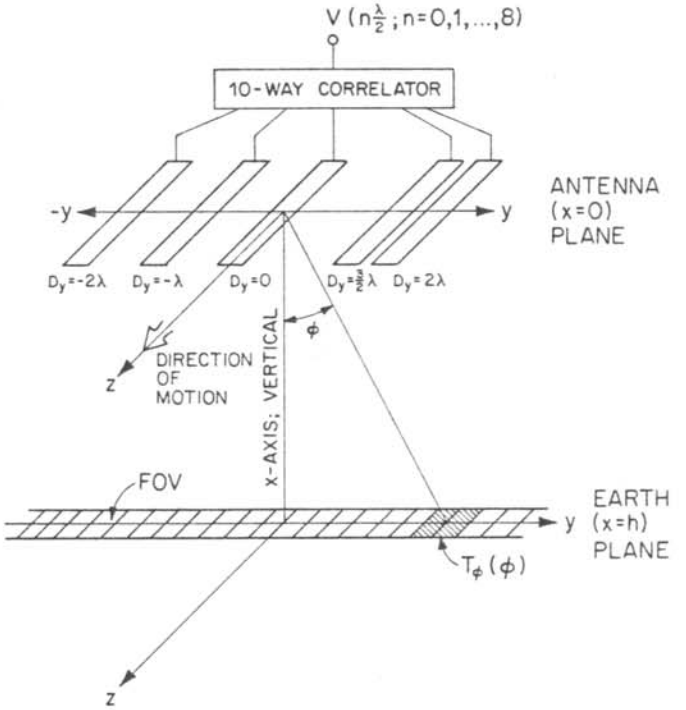

Fig. 3. The ESTAR prototype one-dimensional imaging interferometer—All five antenna elements have coincident fan beam antenna patterns over a strip of the earth. The simultaneous cross-correlation of all pairs of antenna elements produces a Nyquist sampled estimate of the visibility function $V(n(\lambda/2); n = 0, 1, \cdots, 8)$, which is the Fourier transform of the brightness temperature distribution $T_\phi(\phi)$.

Two limiting cases of the redundancy set are a zero redundancy array and a filled array. These cases are described by

Zero Redundancy:

$$r_n = 1 \qquad \text{for } n = 0, 1, \cdots, N$$

Filled Array:

$$r_n = N - n + 1 \qquad \text{for } n = 0, 1, \cdots, N. \quad (25)$$

The zero redundancy array could, for example, result from serially sampling the various antenna spacings with a single pair of antennas. Although not a practical measurement procedure for airborne and spaceborne applications, it serves as an informative limiting case. The filled array consists of a uniform line of $N + 1$ antenna elements at regular, $\lambda/2$, spacings. Thinned linear arrays will, in general, fall somewhere in between these two limits.

The general, two-dimensional imaging fundamentals developed earlier can be specialized to accommodate the ESTAR design. The one-dimensional, ϕ-dependent, brightness temperature distribution that will be imaged is given by

$$T_\phi(\phi) = \int_0^\pi T_{\Omega_{inc}}(\theta, \phi)\, G(\theta, \phi) \sin\theta\, d\theta \quad (26)$$

where

T_ϕ	is in units of K/rad
$T_{\Omega_{inc}}(\theta, \phi)$	is given by (2)
$G(\theta, \phi)$	is approximated by (23)

The brightness temperature measured at each antenna is, then

$$T_B = \int_{-\pi}^{\pi} T_\phi(\phi)\, d\phi. \quad (27)$$

The time varying brightness process (see Appendix I), $b(\phi; t)$, corresponding to the one-dimensional brightness temperature distribution has a power spectral density and autocorrelation respectively described by

$$S_{b(\phi)}(f) = \frac{1}{2B} T_\phi(\phi) \qquad \text{for } f_c - \frac{B}{2} < |f| < f_c + \frac{B}{2}$$
$$= 0 \qquad \text{otherwise} \quad (28)$$

and

$$R_{b(\phi)}(\tau) = T_\phi(\phi) \cos(2\pi f_c \tau)\, \text{sinc}(B\tau) \quad (29)$$

where f_c and B are as in (AI.1). The complex cross-correlation of two of the fan beam antennas will produce a noisy sample of the one-dimensional visibility function. If the antenna pair is spaced $n(\lambda/2)$ apart, $(n = 0, 1, \cdots, N)$, then the expectation of this sample is given by

$$V(n) = \int_{-\pi}^{\pi} T_\phi(\phi) e^{j\pi n \sin\phi}\, d\phi. \quad (30)$$

The one-dimensional image reconstruction formula is

$$\hat{T}_B(\phi) = \sum_{n=-N}^{N} V(n) e^{-j\pi n \sin\phi} \quad (31)$$

where

$$V(-n) = V^*(n); \qquad \text{Hermitian visibility function.}$$

Combining (30) and (31) gives

$$\hat{T}_B(\phi) = \int_{-\pi}^{\pi} T_\phi(\phi')\, AF(\phi, \phi')\, d\phi' \quad (32)$$

where

$$AF(\phi, \phi') = \frac{\sin\left[\pi \dfrac{2N+1}{2} (\sin\phi - \sin\phi')\right]}{\sin\left[\dfrac{\pi}{2} (\sin\phi - \sin\phi')\right]}.$$

Combining (26), (27), and (32), the final brightness temperature estimate at $(\theta = \pi/2, \phi)$, $\hat{T}_B(\phi)$, can be viewed as the brightness temperature measured by a radiometer with an antenna having a directive gain pattern of $G(\theta', \phi')\, AF(\phi, \phi')$

$$\hat{T}_B(\phi) = \int_0^\pi \int_{-\pi}^{\pi} T_{\Omega_{inc}}(\theta', \phi')\, G(\theta', \phi') \cdot AF(\phi, \phi') \sin\theta'\, d\theta'\, d\phi'. \quad (33)$$

The noise floor of the one-dimensional image is found in a manner similar to the two-dimensional derivation, except that redundant samples of the visibility function must be accounted for. From (33) and (34), each visibility sam-

ple $V(n) = V_r(n) + jV_i(n)$, will have a noise floor $\Delta V_{r,i}$ given by

$$\Delta V_{r,i}(n) = \left(\frac{1}{2B\tau}\right)^{1/2} \left[(T_B + T_R)^2 + V_{r,i}^2(n) - V_{i,r}^2(n)\right]^{1/2} \quad (34)$$

where

$T_{R_1} = T_{R_2} = T_R$ is assumed
T_B is given by (27).

Redundant measurements of the same visibility sample can be averaged together to reduce the noise in the estimate of that sample. The degree to which the noise is reduced depends on the statistical dependence of the noise in different measurements. The component of ΔV due to receiver noise T_R is clearly independent for redundant measurements made from different front ends. The dependence of the component of ΔV due to T_B, however, varies with the spacing between the two pairs of antenna elements that are making the redundant measurements. In most cases, and particularly when this spacing is large, the dependence is small and can be ignored. Under these circumstances, the noise floor in the one-dimensional redundancy-averaged image is given by

$$\Delta T(\phi) = \left(\frac{1}{2B\tau}\right)^{1/2} \left\{ \sum_{n=-N}^{N} \frac{1}{r_n} \left[(T_B + T_R)^2 + (V_r^2(n) - V_i^2(n)) \cos(2\pi n \sin\phi)\right] \right\}^{1/2} \quad (35)$$

where

$\{r_n\}_{n=0}^{N}$ *is the appropriate redundancy set;* $r_{-n} = r_n$.

Because the ΔT of the image is dependent on the particular source distribution (through $V(n)$ and T_B), specific examples will be investigated to illustrate the behavior of the noise floor as given by (35).

A homogeneous, uniformly distributed brightness temperature corresponds with the incident brightness temperature distribution given by (5). This will result in a visibility function $V_U(n)$ given by

$$V_U(n) = T_0 \quad \text{for } n = 0$$
$$= 0 \quad \text{otherwise} \quad (36)$$

where T_0 is the uniform brightness temperature (in K). Note that T_0 is also the brightness temperature measured at each antenna (T_B in (35)). Under this condition, the noise floor will reduce to

$$\Delta T_U = \left(\frac{1}{2B\tau}\right)^{1/2} \left\{ \left[\frac{1}{r_0}\left((T_0 + T_R)^2 + T_0^2\right)\right]^{1/2} + (T_0 + T_R)\left(2\sum_{n=1}^{N}\frac{1}{r_n}\right)^{1/2} \right\}. \quad (37)$$

For high resolution imaging ($N >> 1$), (37) can be further reduced for specific array configurations. In the zero redundancy case, the noise floor becomes

$$\Delta T_{U-Z} = (T_0 + T_R)\left(\frac{N}{B\tau}\right)^{1/2}. \quad (38)$$

For the filled array, the ΔT is given by

$$\Delta T_{U-F} = (T_0 + T_R)\left(\frac{C + \ln N}{B\tau}\right)^{1/2} \quad (39)$$

where

$$\sum_{n=0}^{N-1}\frac{1}{N-n} \approx C + \ln N;$$

$C = 0.5772 \cdots$ is Euler's Constant.

Although the noise floor increases in both cases with N, it does so much more slowly with the filled array, for which the redundant samples greatly reduce the effects of measurement noise. Note that, because the filled array ΔT still grows with N, it is not comparable to a conventional filled phased array, which performs its detection process after a phased voltage combination of the signals from all the antennas.

A point source brightness temperature distribution should produce a nonzero brightness temperature estimate at one location in the image. This is provided by the following distribution:

$$T_\phi^p(\phi) = \frac{1}{2N+1} T_0 \delta(\phi - \hat{\phi}) \quad (40)$$

where

T_ϕ is in units of K/rad
$\hat{\phi}$ is the location of the point source.

The corresponding brightness temperature measured by an individual antenna (T_B in (27)) is, then

$$T_B^p = \int_{-\pi}^{\pi} T_\phi^p(\phi)\, d\phi = \frac{1}{2N+1} T_0. \quad (41)$$

The visibility function $V_p(n)$ resulting from this distribution is found from (30)

$$V_p(n) = \frac{1}{2N+1} T_0 e^{j\pi n \sin\hat{\phi}}. \quad (42)$$

The estimated brightness temperature of the image at $\hat{\phi}$ is given by (32) as

$$\hat{T}_B(\hat{\phi}) = \frac{1}{2N+1} T_0 AF(\hat{\phi}, \hat{\phi}) = T_0. \quad (43)$$

It is the result in (43) that motivated the initial $1/2N + 1$ normalization in (40). This normalization also corresponds physically to a patch of radiating earth of brightness temperature T_0 covering $(1/2N + 1)$th of the FOV. The noise floor present in the estimate of $T_B(\phi)$ in

the point source image is found by combining (35), (41), and (42). For a high-resolution zero redundancy imager, this ΔT becomes

$$\Delta T_{p-Z} = T_R\left(\frac{N}{B\tau}\right)^{1/2}. \tag{44}$$

For high-resolution filled array imaging, the noise floor is

$$\Delta T_{p-F} = T_R\left(\frac{C + \ln N}{B\tau}\right)^{1/2}. \tag{45}$$

Note that the contribution to the noise floor from the brightness temperature distribution itself is negligible under the assumptions that $N \gg 1$ and the source is small. In such cases, the equivalent receiver noise temperature of the cross-correlators is the dominant source of noise in the image.

In actual implementations of the ESTAR imager, the magnitude of the typical brightness temperature distributions under observation will be on the order of the equivalent receiver noise temperature across the entire FOV. In many applications, they will also tend to be relatively uniform (e.g., open oceans or inland vegetation or soil). In these cases, the ESTAR ΔT can be approximated from (37) by

$$\Delta T_{\text{ESTAR}} = (T_B + T_R)\left(\frac{\sum_{n=0}^{N} 1/r_n}{B\tau}\right)^{1/2} \tag{46}$$

where

T_B is given by (27).

Equation (46) explicitly states the critical effect that the distribution of redundancies has on the performance of a thinned array imager. It is in general best to distribute these redundancies as evenly as possible over all relative antenna spacings in order to maximize their effect on the reduction of noise in the final image. For example, if a given potential thinned array configuration will not provide the ΔT resolution required by a user, then additional fan beam elements can be added to the configuration in judicious places to reduce the ΔT of the image. The placement of these elements would be chosen so as to minimize (46) or, equivalently, to generate new redundancies at spacings with the fewest previous samples. In cases where the brightness temperature distribution is neither uniform nor a point source, the noise floor in the image should be determined using (35). In such cases, the placement of redundant antenna elements can at best accommodate some average, expected distribution.

V. Large Spaceborne ESTAR Antennas

The best arrangement of antenna elements in the ESTAR prototype array described in the previous section can be determined in a straightforward manner because of the low number of elements involved. With five elements, simple trial and error will quickly determine the minimum redundancy array configuration. The minimum redundancy arrangement for a large number of antenna elements is much more difficult to find. This problem received early attention as an abstract problem in mathematical number theory [12], [13]. Leech provides an algorithm for constructing a low redundancy array configuration and Ruzsa tightens previous upper and lower bounds on the number of elements required to form a minimum redundancy array, for very large numbers. However, there is no available algorithm that specifies the placement of antenna elements in an optimally thinned array of arbitrary size.

The Leech algorithm can be incorporated into modern high-speed computers to aid in locating the elements of large thinned arrays. For example, a 32-element array capable of sampling the visibility function out to a maximum spacing of $256(\lambda/2)$ was determined by the authors after approximately 100 h of CPU time on a VAX 11/750. An alternative technique for locating the array elements has been developed by [14]. This method uses the optimal configurations determined for small arrays to build thinned arrays of thinned arrays. The elements of the "sub-arrays" are individual antenna elements with a $\lambda/2$ inter-element unit spacing. The elements of the "super-array" are the sub-arrays, configured according to the optimal thinning determined by the number of sub-arrays and spaced in units of $(2N + 1)\lambda/2$, where $N(\lambda/2)$ is the maximum spacing in one sub-array. For example, five six-element sub-arrays will Nyquist sample the visibility function out to a maximum spacing of $256(\lambda/2)$ using $5 \times 6 = 30$ antenna elements. This is an improvement by two elements over the Leech algorithm. Thinned array configurations with a maximum spacing of $16(\lambda/2)$, $64(\lambda/2)$, $256(\lambda/2)$, and $1032(\lambda/2)$, derived by the above techniques, are described in Table I.

The spatial resolution of a thinned array imager is determined by its maximum relative antenna spacing. The temperature resolution, or ΔT, of the image is determined by the total array configuration, as given by (46) when imaging a uniform brightness temperature distribution from low earth orbit. This expression represents a degradation in the ΔT performance of a nonscanning, real aperture pencil beam measurement by a factor of $(\Sigma_{n=0}^{N} 1/r_n)^{1/2}$. This degradation factor is computed in Table II for several zero redundancy, thinned array, and filled array redundancy sets. The thinned array configurations used are those given in Table I. In Table II, the thinned arrays perform only slightly better than the worst case, zero redundancy, arrays. This is an indication that these arrays are nearly optimally thinned. The degradation in the performance of the filled arrays, on the other hand, is small even with 1032 elements. This was suggested by the very slowly growing degradation factor $(C + \ln N)^{1/2}$ given by (39). A partially filled thinned array will operate somewhere in between these performance limits, depending on the form of its redundancy set. The rate at which partial filling improves on the performance of a thinned array is demonstrated in Fig. 4.

TABLE I
THINNED ARRAY SPECIFICATIONS

Number of Elements	Maximum Spacing ($\times \frac{\lambda}{2}$)	Approximate Spatial Resolution from Low Earth Orbit
7	16	122 km
14	64	31 km
30	256	8 km
63	1032	2 km

Antenna Element Locations (given in units of $\frac{\lambda}{2}$)

7 element (minimum redundancy)

0,1,2,3,8,12,16

14 element (Leech algorithm)

0,1,2,3,4,29,30,36,41,46,51,56,60,64

30 element (Ishiguro 6x5)

0,1,6,9,11,13,27,28,33,36,38,40,108,109,114,117,119,121,189,190,195,198,200, 202,243, 244,249,252,254,256

63 element (Ishiguro 9x7)

0,1,4,10,16,22,24,27,29,59,60,63,69,75,81,83,86,88,236,237,240,246,252,258, 260,263, 265,590,591,594,600,606,612,614,617,619,708,709,712,718,724,730,732,735,737, 885, 886,889,895,901,907,909,912,914,1003,1004,1007,1013,1019,1025,1027,1030,1032

TABLE II
THINNED ARRAY ΔT DEGRADATION

Maximum Spacing ($\times \frac{\lambda}{2}$)	ΔT Degradation $\triangleq \frac{\Delta T}{(T_B+T_R)/\sqrt{Bt}}$ or $(\sum_{n=0}^{N} \frac{1}{r_n})^{1/2}$		
	Zero Redundancy[1]	Thinned Array	Filled Array[2]
16	4.13	3.73[3]	1.85
64	8.06	7.42[4]	2.18
256	16.04	14.41[5]	2.47
1032	32.15	27.93[6]	2.74

1 - Worst Case ΔT; $r_n = 1$ for $n = 0, 1, \cdots, N$

2 - Best Case ΔT; $r_n = N - n + 1$

3 - 7 element minimum redundancy array

4 - 14 element Leech/UMass thinned array

5 - 30 element Ishiguro array

6 - 63 element Ishiguro array

The degradation factor is plotted for partially filled arrays of various sizes. The placement of additional antenna elements is in all cases chosen so as to minimize the degradation factor. Note that the greatest improvement in system performance occurs as the thinned array first begins to fill in.

The attraction of synthetic aperture radiometry in low earth orbit is evident from these array examples. A 30-element Ishiguro array would produce images with a spatial resolution comparable to that of a 128λ-by-128λ real aperture while using only 12 percent of the physical aperture. This corresponds to 8-km resolution from 30 27 m × 11 cm antenna sticks at 1.4 GHz. With 63 elements, the spatial resolution becomes 2 km and the savings in physical aperture is improved to 6 percent of the equivalent real aperture.

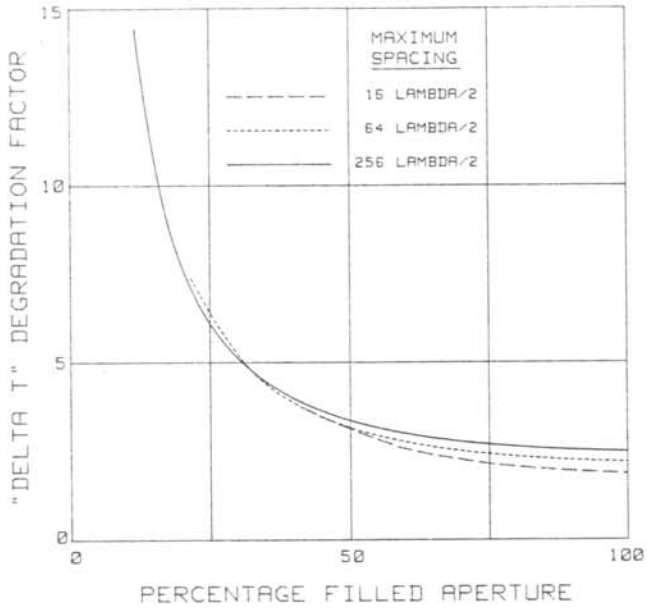

Fig. 4. ΔT improvement by partial filling of thinned arrays—Low redundancy thinned arrays are filled by adding additional elements where they will reduce the ΔT degradation the most. The majority of this reduction occurs in the early stages of filling.

The utility of brightness temperature images of the earth is in many applications strongly dependent on the ΔT of that image. For example, a 1.4-GHz imager would require approximately $\Delta T \leq 1.0$ K to estimate soil moisture content within 0.5 percent by weight [15]. Using typical system parameters in low earth orbit ($T_B = T_R = 300$ K, $B = 30$ MHz, Altitude = 800 km) and the Ishiguro 30-element array with a spatial resolution of 8 km, $\Delta T = 2.1$ K. For the same system parameters and a filled array, the ΔT becomes 0.4 K. A partially filled array capable of producing images with a 1.0 K noise floor is determined from Fig. 4 to require a 25-percent filled aperture.

VI. EARTH REMOTE SENSING VERSUS RADIO ASTRONOMY

Passive microwave remote sensing of the earth typically involves a large, radiometrically bright, FOV filled with a distributed source, which is viewed from a moving platform for a relatively short period of time. Radio astronomy, on the other hand, often utilizes hours of earth rotation to map out the *uv*-plane, does so from large, permanent, ground-based stations, and concerns itself with very narrow FOV's that often contain weak, isolated sources. These differences are central to the successful application of radio astronomy techniques to earth remote sensing.

The particular source distribution imaged by interfero-

metric aperture synthesis can strongly influence the noise floor of the image. However, if the source under observation covers a small part of the total FOV, or if the equivalent receiver noise temperature is much larger than the brightness temperature of the complete FOV (T_B measured by one antenna element), then the image sensitivity reduces to that given by (44) for a zero-redundancy array. Note that this noise floor is independent of the source brightness temperature even if it is much brighter than the receiver noise, provided the source is small (relative to the synthesized resolution) and the resolution is high ($N \gg 1$). These conditions are typical of radio astronomical observations. Early analysis of the image sensitivity of radio interferometers relied on the high receiver noise to argue toward this result [16]. More recent derivations, for which the receiver noise has been substantially reduced by improved technology, have based their results on the assumption of a small source [17]. In either case, the result given by (44) can be rewritten in the flux density-dependent nomenclature typical of the radio astronomy literature by incorporating the conversion scheme outlined by (1)–(4)

$$\Delta S = \frac{2kT_R}{nA_e\sqrt{B\tau}} \tag{47}$$

where

- ΔS is the detectable change in flux density at the antennas due to a change in the imaged source (in units of $W/m^2 - Hz - sr$-synthesized beam).
- n is the number of antennas ($\approx \sqrt{2N}$ for a zero redundancy array).
- A_e is the effective aperture of one antenna element (in m^2).

Equation (47) is consistent with the results cited above. It has commonly been interpreted as a relationship between the sensitivity and the total collecting area ($= nA_e$) of an imager. However, this connection is, in general, not valid for earth remote-sensing purposes.

The requirements for the validity of (44) and (47) would usually not be true of an earth viewing synthetic imager. Bright source distributions typically fill the entire FOV and zero redundancy arrays are not practical on an orbiting platform. The array configurations used should, therefore, not be determined solely by the total collecting area they provide. The distribution of visibility samples that they generate across the redundancy set ought also to be considered, as outlined in the previous section.

One aspect of the effect that an extended source has on the sensitivity of the image has been addressed in the radio astronomy literature [18]. In this context, an extended source is any brightness temperature distribution that is larger than the synthesized resolution of the image. As the resolution increases, correspondingly less flux is intercepted by the antennas per unit synthesized beam. This serves to increase the noise floor as the resolution increases. However, the effects of the change in visibility function due to the extended source on the noise floor (as prescribed by (35)) are not taken into account. That this omission still permits satisfactory predictions of the image noise floor suggests that either the FOV is still substantially larger than the "extended" source distribution, or the receiver noise is dominant, or both. In the case of an earth viewing imager, of course, the source distribution is usually "extended" to the point of filling the entire FOV. However, the increase in noise floor with resolution noted by the radio astronomers does not apply to the ΔT equations derived above. The dependence of incident flux density at the antennas on various distributed portions of the FOV has already been incorporated into the defining properties of the brightness temperature distributions $T_\Omega(\theta, \phi)$ and $T_\phi(\phi)$.

The nature of the sources typically imaged for radio astronomical purposes also enters into earth remote sensing in one other way. As mentioned earlier, radio astronomy interferometers often dwell on a particular, highly localized, source distribution for a period of hours. This is accomplished by mechanically steering the antenna elements to keep the source within their FOV. The long integration time (τ in (47)) improves the sensitivity of the image. The many different relative antenna spacings generated as the earth rotates during this dwell time also sample different points on the uv-plane. Most importantly for our purposes, the concentration on a relatively small region of the sky allows differential time delays to be introduced into the individual antenna channels prior to their cross-correlation to account for deviations of the locations of the antenna elements from a true plane that is perpendicular to the incident radiation. This correction prevents the incident noise being measured from decorrelating between antennas. For example, a thermal noise process filtered to a bandwidth of 100 MHz (typical for radio astronomy or earth remote sensing) has a decorrelation length in air of approximately 3 m. The cross-correlation of signals from antennas that vary by an appreciable percentage of this decorrelation length from the true perpendicular plane mentioned above would be degraded by the decorrelation of the signals. This degradation is known as fringe washing [18].

The derivation of interferometric imaging fundamentals presented earlier implicitly ignored the effects of fringe washing (see discussion following (AI.8)). These effects will, however, degrade the performance of the imager at a point in the FOV if the difference in pathlength from that point to any two of the antenna pairs is an appreciable percentage of the decorrelation length of the bandlimited thermal emission. This degradation will become significant as the antenna structures approach the dimensions required for sub-10-km resolution from low earth orbit at microwave frequencies. The differential time delay corrections available to the radio astronomer will not work over the wide instantaneous FOV imaged by an earth viewing interferometer. One possible solution, presently under investigation by the authors, is a division of the full RF bandwidth into a bank of narrower channels, each with a much longer decorrelation length, which can be recom-

bined after image reconstruction to reduce the noise floor of the composite image.

Finally, while there are certainly numerous important differences between the implementation of aperture synthesis techniques for astronomical studies and for the remote sensing of the earth, the similarities are much more significant. There is a wealth of engineering research available to the earth remote-sensing community to aid in the adaptation of synthetic aperture radiometry to their needs. The radio astronomy references cited in this paper are general reviews of the performance characteristics of interferometric radio telescopes. There is a large body of additional documentation on specific hardware instrumentation and calibration, and image reconstruction and enhancement "nuts and bolts" which should help enormously in overcoming the inevitable engineering pitfalls that will be encountered by this developing technology.

Appendix I
Derivation of the Visibility Function

The incident radiation described in Part I was characterized only in terms of its power content because of the statistical nature of the thermal emission involved. The stochastic process giving rise to these statistics corresponds to the voltage time series generated at the antenna terminals. Let $v_B(t)$ be this voltage. Its power spectral density is given by

$$S_{v_B}(f) = \frac{kZ_0T_B}{2} \quad \text{for } f_c - \frac{B}{2} < |f| < f_c + \frac{B}{2}$$
$$= 0 \quad \text{otherwise} \qquad \text{(AI.1)}$$

where

- S_{v_B} is in units of V^2/Hz
- Z_0 is the characteristic impedance at the antenna terminals
- T_B is given by (4)
- f_c is the RF center frequency of the signal

A rectangular RF bandpass window is assumed.

It is convenient to express the voltage process $v_B(t)$ in units of $K^{1/2}$, which differs from volts only by a constant of proportionality. To this end, define the brightness temperature equivalent stochastic process (brightness process) $b(t)$ by

$$b(t) = (kBZ_0)^{-1/2} v_B(t). \qquad \text{(AI.2)}$$

Its power spectral density (in units of K/Hz) follows as:

$$S_b(f) = \frac{1}{2B} T_B \quad \text{for } f_c - \frac{B}{2} < |f| < f_c + \frac{B}{2}$$
$$= 0 \quad \text{otherwise.} \qquad \text{(AI.3)}$$

This brightness process can be decomposed in the same manner as was the brightness temperature T_B in Part I into its sources over the FOV observed by the antenna. Let $\beta(\theta, \phi; t)$ be the baseband brightness process per steradian at the source of the thermal emission. Its power spectral density (in units K/sr − Hz) is

$$S_{\beta(\theta,\phi)}(f) = \frac{2}{B} T_\Omega(\theta, \phi) \quad \text{for } |f| < \frac{B}{2}$$
$$= 0 \quad \text{otherwise} \qquad \text{(AI.4)}$$

where

the factor of 2 accounts for spectral foldover at dc
$T_\Omega(\theta, \phi)$ is given by (3)

The RF (passband) brightness process per steradian at the source is $\beta(\theta, \phi; t) \cos(2\pi f_c t)$. The corresponding brightness process per steradian at the antenna $b(\theta, \phi; t)$ follows as:

$$b(\theta, \phi; t) = \beta(\theta, \phi; t) \cos\left[2\pi f_c t - kr(\theta, \phi)\right] \qquad \text{(AI.5)}$$

where

- $b(\theta, \phi, t)$ is in units of $K^{1/2}/sr$
- $k = 2\pi/\lambda$; $\lambda = c/f_c$
- $r(\theta, \phi)$ is the pathlength from the source at (θ, ϕ) to the antenna.

The power spectral density of $b(\theta, \phi; t)$ (in units of K/sr − Hz) is

$$S_{b(\theta,\phi)}(f) = \frac{1}{2B} T_\Omega(\theta, \phi) \quad \text{for } f_c - \frac{B}{2} < |f| < f_c + \frac{B}{2}$$
$$= 0 \quad \text{otherwise.} \qquad \text{(AI.6)}$$

The brightness process $b(t)$ then follows by integrating $b(\theta, \phi; t)$ over all solid angles. Note that $b(t)$ will be modeled as additive Gaussian noise.

Returning to Fig. 1, if $r(\theta, \phi)$ is the distance from a point on the earth to antenna #1, and $r'(\theta, \phi)$ is the distance to antenna #2, then the brightness processes at the two antennas are given by

$$b_1(t) = \int_0^{2\pi} \int_0^{\pi} \beta(\theta, \phi; t) \cos\left[2\pi f_c t - kr(\theta, \phi)\right] \cdot \sin\theta \, d\theta \, d\phi \qquad \text{(AI.7)}$$

$$b_2(t) = \int_0^{2\pi} \int_0^{\pi} \beta(\theta, \phi; t) \cos\left[2\pi f_c t - kr'(\theta, \phi)\right] \cdot \sin\theta \, d\theta \, d\phi. \qquad \text{(AI.8)}$$

It should be noted that (AI.7) and (AI.8) are only valid provided the baseband brightness process $\beta(\theta, \phi; t)$ has suffered little decorrelation between the two antennas. This is equivalent to assuming that $\beta(\theta, \phi; t - [r(\theta, \phi) - r'(\theta, \phi)]/c) \approx \beta(\theta, \phi; t)$ for all (θ, ϕ) in the FOV. Cases in which the noise decorrelation is not negligible were addressed in Part VI.

An interferometer measurement is made by a complex cross-correlation of $b_1(t)$ with $b_2(t)$. The real and imag-

inary components of this correlation are given by

$$\operatorname{Re}\left\{V(D_x, D_y)\right\} = \langle b_1(t)\, b_2(t)\rangle$$

$$\operatorname{Im}\left\{V(D_x, D_y)\right\} = \left\langle b_1(t)\, b_2\left(t - \frac{1}{4f_c}\right)\right\rangle \quad \text{(AI.9)}$$

where

$V(D_x, D_y)$ is the visibility function (correlator output) in units of K

D_x and D_y are the relative antenna locations

$b_2(t - 1/4f_c) \approx \int_0^{2\pi}\int_0^{\pi} \beta(\theta, \phi; t) \sin[2\pi f_c t - kr'(\theta, \phi)] \sin\theta\, d\theta\, d\phi$ (valid for $B \ll f_c$)

$\langle \cdot \rangle$ denotes the expectation operator.

Equation (AI.9) can be rewritten in terms of the brightness temperature distribution $T_\Omega(\theta, \phi)$ by recognizing that the autocorrelation of $\beta(\theta, \phi; t)$, $R_{\beta(\theta,\phi)}(\tau)$ is the Fourier transform of its power spectral density [19]

$$R_{\beta(\theta,\phi)}(\tau) = \langle \beta(\theta, \phi; t)\, \beta(\theta, \phi; t + \tau)\rangle = 2T_\Omega(\theta, \phi)\operatorname{sinc}(B\tau) \quad \text{(AI.10)}$$

where

$$\operatorname{sinc}(x) = \frac{\sin \pi x}{\pi x}.$$

Using (AI.7), (AI.8), and (AI.10), and making the approximation $r'(\theta, \phi) - r(\theta, \phi) \approx D_x \sin\theta \cos\phi + D_y \sin\theta \sin\phi$ (valid for $r >> D_x, D_y$), (AI.9) becomes

$$V(u, v) = \int_0^{2\pi}\int_0^{\pi} T_\Omega(\theta, \phi) e^{j2\pi(u\sin\theta\cos\phi + v\sin\theta\sin\phi)} \cdot \sin\theta\, d\theta\, d\phi \quad \text{(AI.11)}$$

where

$$u = \frac{D_x}{\lambda},\ v = \frac{D_y}{\lambda}.$$

Appendix II
Standard Deviation of Visibility Samples

Referring to Fig. 2 and (AI.7)–(AI.10), (10), and (11), let the time varying processes entering the integrators after the multiplication with and without the 90° phase shifter acting on one of the multiplicands be given by $m_r(t)$ and $m_i(t)$, respectively. These processes are described by

$$m_r(t) = [b_1(t) + n_1(t)][b_2(t) + n_2(t)] \quad \text{(AII.1)}$$

$$m_i(t) = [b_1(t) + n_1(t)] \cdot \left[b_2\left(t - \frac{1}{4f_c}\right) + n_2\left(t - \frac{1}{4f_c}\right)\right]. \quad \text{(AII.2)}$$

The autocorrelation of these processes follows as:

$$\begin{aligned} R_{m_r}(\tau) &= \langle m_r(t)\, m_r(t + \tau)\rangle \\ &= \langle b_1(t)\, b_2(t)\rangle^2 + \langle b_1(t)\, b_1(t + \tau)\rangle \cdot \langle b_2(t)\, b_2(t + \tau)\rangle + \langle b_1(t)\, b_2(t + \tau)\rangle \\ &\quad \cdot \langle b_2(t)\, b_1(t + \tau)\rangle + \langle n_1(t)\, n_1(t + \tau)\rangle \cdot \langle n_2(t)\, n_2(t + \tau)\rangle + \langle b_1(t)\, b_1(t + \tau)\rangle \\ &\quad \cdot \langle n_2(t)\, n_2(t + \tau)\rangle + \langle b_2(t)\, b_2(t + \tau)\rangle \cdot \langle n_1(t)\, n_1(t + \tau)\rangle \\ &= V_r^2(u, v) + \operatorname{sinc}^2(B\tau)[(T_B + T_{R_1}) \cdot (T_B + T_{R_2}) \cdot \cos^2(2\pi f_c\tau) + V_r^2(u, v) \\ &\quad \cdot \cos^2(2\pi f_c\tau) - V_i^2(u, v)\sin^2(2\pi f_c\tau)] \\ &= V_r^2(u, v) + \tfrac{1}{2}\operatorname{sinc}^2(B\tau)[(T_B + T_{R_1}) \cdot (T_B + T_{R_2}) + V_r^2(u, v) - V_i^2(u, v)] \\ &\quad + \tfrac{1}{2}\operatorname{sinc}^2(B\tau)\cos(4\pi f_c\tau)[(T_B + T_{R_1}) \cdot (T_B + T_{R_2}) + V_r^2(u, v) + V_i^2(u, v)] \end{aligned} \quad \text{(AII.3)}$$

where the following relations have been used:

$$\begin{aligned} \langle b_1(t)\, b_1(t + \tau)\rangle &= \langle b_2(t)\, b_2(t + \tau)\rangle = T_B \operatorname{sinc}(B\tau)\cos(2\pi f_c\tau) \\ \langle b_1(t)\, b_2(t + \tau)\rangle &= \operatorname{sinc}(B\tau)[\cos(2\pi f_c\tau)V_r(u, v) + \sin(2\pi f_c\tau)V_i(u, v)] \\ \langle b_2(t)\, b_1(t + \tau)\rangle &= \operatorname{sinc}(B\tau)[\cos(2\pi f_c\tau)V_r(u, v) - \sin(2\pi f_c\tau)V_i(u, v)] \\ \langle b_1(t)\, b_2(t)\rangle &= V_r(u, v) \\ \langle n_1(t)\, n_1(t + \tau)\rangle &= T_{R_1}\operatorname{sinc}(B\tau)\cos(2\pi f_c\tau) \\ \langle n_2(t)\, n_2(t + \tau)\rangle &= T_{R_2}\operatorname{sinc}(B\tau)\cos(2\pi f_c\tau). \end{aligned}$$

Similarly

$$\begin{aligned} R_{m_i}(\tau) &= V_i^2(u, v) + \tfrac{1}{2}\operatorname{sinc}^2(B\tau)[(T_B + T_{R_1}) \cdot (T_B + T_{R_2}) + V_i^2(u, v) - V_r^2(u, v)] \\ &\quad + \tfrac{1}{2}\operatorname{sinc}^2(B\tau)\cos(4\pi f_c\tau)[(T_B + T_{R_1}) \cdot (T_B + T_{R_2}) + V_i^2(u, v) + V_r^2(u, v)]. \end{aligned} \quad \text{(AII.4)}$$

The power spectral densities of m_r and m_i are the Fourier transforms of (AII.3) and (AII.4). Rejecting the term modulated by $\cos 4\pi f_c\tau$, which will not pass through the

subsequent lowpass filter, these spectra are given by

$$S_{m_r}(f) = V_r^2(u, v)\,\delta(f) + \tfrac{1}{2}T(f)\left[(T_B + T_{R_1}) \cdot (T_B + T_{R_2}) + V_r^2(u, v) - V_i^2(u, v)\right] \quad \text{(AII.5)}$$

$$S_{m_i}(f) = V_i^2(u, v)\,\delta(f) + \tfrac{1}{2}T(f)\left[(T_B + T_{R_1}) \cdot (T_B + T_{R_2}) + V_i^2(u, v) - V_r^2(u, v)\right] \quad \text{(AII.6)}$$

where

$$T(f) = \frac{1}{B}\left(1 - \left|\frac{f}{B}\right|\right) \quad \text{for } |f| < B$$
$$= 0 \quad \text{otherwise}$$

is the convolution of the Fourier transfer of sinc $(B\tau)$ with itself.

The processes $m_r(t)$ and $m_i(t)$ are passed through lowpass filters with transfer functions $H_{LP}(f)$, given by (11), to produce noisy samples of the real and imaginary components of the visibility function, given by $V_r(u, v; t)$ and $V_i(u, v; t)$, respectively. Their power spectral densities are

$$S_{V_{r,i}}(f) = S_{m_{r,i}}(f)\left|H_{LP}(f)\right|^2. \quad \text{(AII.7)}$$

$T(f)$ can be approximated by its value at dc $(f = 0)$ across the bandwidth of the lowpass filters. This simplifies the expression for the power spectral densities of the visibility samples to

$$S_{V_{r,i}}(f) = V_{r,i}^2(u, v)\,\delta(f) + \frac{1}{2B}\left[(T_B + T_{R_1}) \cdot (T_B + T_{R_2}) + V_{r,i}^2(u, v) - V_{i,r}^2(u, v)\right] \quad \text{for } |f| < \frac{1}{2\tau}$$
$$= 0 \quad \text{otherwise.} \quad \text{(AII.8)}$$

This expression can be rewritten as

$$S_{V_r(u,v)}(f) = S^{DC}_{V_r(u,v)} + S^{AC}_{V_r(u,v)}(f)\ \mathrm{K^2/Hz} \quad \text{(AII.9)}$$

$$S_{V_i(u,v)}(f) = S^{DC}_{V_i(u,v)} + S^{AC}_{V_i(u,v)}(f)\ \mathrm{K^2/Hz} \quad \text{(AII.10)}$$

where a decomposition into ac and dc components has been performed. These components are given by

$$S^{DC}_{V_r(u,v)} = V_r^2(u, v)\,\delta(f) \quad \text{(AII.11)}$$

$$S^{AC}_{V_r(u,v)}(f) = \frac{1}{2B}\left[(T_B + T_{R_1})(T_B + T_{R_2}) + V_r^2(u, v) - V_i^2(u, v)\right] \quad \text{for } |f| < \frac{1}{2\tau}$$
$$= 0 \quad \text{otherwise} \quad \text{(AII.12)}$$

$$S^{DC}_{V_i(u,v)} = V_i^2(u, v)\,\delta(f) \quad \text{(AII.13)}$$

$$S^{AC}_{V_i(u,v)}(f) = \frac{1}{2B}\left[(T_B + T_{R_1})(T_B + T_{R_2}) + V_i^2(u, v) - V_r^2(u, v)\right] \quad \text{for } |f| < \frac{1}{2\tau}$$
$$= 0 \quad \text{otherwise} \quad \text{(AII.14)}$$

where

$V_r(u, v) = \int_0^{2\pi}\int_0^{\pi} T_\Omega(\theta, \phi)\cos\left[2\pi(u \sin\theta\cos\phi + v \sin\theta\sin\phi)\right]\sin\theta\, d\theta\, d\phi$
$V_i(u, v) = \int_0^{2\pi}\int_0^{\pi} T_\Omega(\theta, \phi)\sin\left[2\pi(u \sin\theta\cos\phi + v \sin\theta\sin\phi)\right]\sin\theta\, d\theta\, d\phi$
$T_B = V_r(u = 0, v = 0)$
$\delta(x)$ is the Dirac delta function
All power spectral densities are in units of $\mathrm{K^2/Hz}$.

The change in the dc power level of the noisy samples, $V_{r,i}(u, v; t)$, which results from an incremental change by $\Delta V_{r,i}(u, v)$ in the components of the true visibility function, is given by

$$\Delta\mathrm{Power}^{DC}_{r,i} = \int_{-\infty}^{\infty} S^{DC}_{V_{r,i}(u,v)}\Big|_{V_{r,i}(u,v)=\Delta V_{r,i}} df. = \Delta V_{r,i}^2(u, v). \quad \text{(AII.15)}$$

The power level of the noise in the sample itself is correspondingly found by integrating the ac component of its power spectral density over all frequencies

$$\mathrm{Power}^{AC}_{r,i} = \int_{-\infty}^{\infty} S_{V_{r,i}(u,v)}(f)\, df$$

or

$$\mathrm{Power}^{AC}_{r} = \frac{1}{2B\tau}\left[(T_B + T_{R_1})(T_B + T_{R_2}) + V_r^2(u, v) - V_i^2(u, v)\right]$$

$$\mathrm{Power}^{AC}_{i} = \frac{1}{2B\tau}\left[(T_B + T_{R_1})(T_B + T_{R_2}) + V_i^2(u, v) - V_r^2(u, v)\right]. \quad \text{(AII.16)}$$

The standard deviations in the visibility samples $\Delta V_{r,i}$ are defined by equating (AII.15) and (AII.16) [10]

$$\Delta V_r(u, v) = \left(\frac{1}{2B\tau}\right)^{1/2}\left[(T_B + T_{R_1})(T_B + T_{R_2}) + V_r^2(u, v) - V_i^2(u, v)\right]^{1/2}\mathrm{K} \quad \text{(AII.17)}$$

$$\Delta V_i(u, v) = \left(\frac{1}{2B\tau}\right)^{1/2}\left[(T_B + T_{R_1})(T_B + T_{R_2}) + V_i^2(u, v) - V_r^2(u, v)\right]^{1/2}\mathrm{K} \quad \text{(AII.18)}$$

REFERENCES

[1] T. T. Wilheit and A. T. C. Chang, "An algorithm for retrieval of ocean surface and atmospheric parameters from the observations of the scanning multichannel microwave radiometer," *Radio Sci.*, vol. 15, pp. 525–544, 1980.

[2] G. C. Thomann, "Experimental results of the remote sensing of sea-surface salinity at 21-cm wavelength," *IEEE Trans. Geosci. Electron.*, vol. GE-14, pp. 198–214, 1976.

[3] C. T. Swift, "Microwave radiometer measurements of the Cape Cod canal," *Radio Sci.*, vol. 9, pp. 641–653, 1974.

[4] J. R. Wang *et al.*, "Multifrequency measurements of the effects of soil moisture, soil texture, and surface roughness," *IEEE Trans. Geosci. Remote Sensing*, vol. GE-21, pp. 44–51, 1983.

[5] C. T. Swift *et al.*, "An algorithm to measure sea ice concentration with microwave radiometers," *J. Geophys. Res.*, vol. 90, pp. 1087–1099, 1985.

[6] C. T. Swift, "High resolution passive microwave imaging of the surface of the earth," NASA Ref. Pub. 1079, pp. 33–41, 1981.

[7] N. Skou, "Push-broom microwave radiometer systems for space applications," in *Proc. IGARSS*, 1985.

[8] J. L. Pawsey and R. N. Bracewell, *Radio Astronomy*. London: Oxford, 1955.

[9] P. J. Napier *et al.*, "The very large array: design and performance of a modern synthesis radio telescope," *Proc. IEEE*, vol. 71, no. 11, Nov. 1983.

[10] G. Evans and C. W. McLeish, *RF Radiometer Handbook*. Dedham, MA: Artech House, 1977.

[11] A. T. Moffett, "Minimum-redundancy linear arrays," *IEEE Trans. Antennas Propagat.*, vol. AP-16, pp. 172–175, 1968.

[12] J. Leech, "On the representation of 1, 2, $\cdots$, n by differences," *J. London Math. Soc.*, vol. 31, pp. 160–169, 1956.

[13] I. Z. Ruzsa, "On difference-sequences," *Acta Arithmetica*, vol. XXV, pp. 151–157, 1974.

[14] M. Ishiguro, "Minimum redudancy linear arrays for a large number of antennas," *Radio Sci.*, vol. 15, pp. 1163–1170, 1980.

[15] T. J. Schmugge, "Effect of texture on microwave emission from soil," *IEEE Trans. Geosci. Electron.*, vol. GE-18, pp. 353–361, 1980.

[16] W. N. Christiansen and J. A. Högbom, *Radiotelescopes*. Cambridge, England: Cambridge Univ. Press, 1969, ch. 8, pg. 203.

[17] P. J. Napier and P. C. Crane, "Signal-to-noise ratios," in *Proc. NRAO Workshop No. 5, Synthesis Mapping* (NRAO, Socorro, NM), pp. 3–6, June 1982.

[18] E. B. Fomalont and C. H. Wright, *Golactic and Extragalactic Radio Astronomy*, G. L. Vershwr and K. I. Kellermann, Eds. New York: Springer-Verlag, 1974, ch. 10, pp. 276–277.

[19] A. Papoulis, *Probability, Random Variables, and Stochastic Processes*. New York: McGraw-Hill, 1984.

*

Christopher S. Ruf (S'85–M'87) received the B.A. degree in physics from Reed College, Portland, OR in 1982 and the Ph.D. degree in electrical and computer engineering from the University of Massachusetts, Amherst in 1987.

He is currently completing a one year appointment as Visiting Professor and Research Engineer at the University of Massachusetts. His research interests are in microwave interferometric spatial imaging instrumentation, microwave autocorrelation spectral imaging instrumentation, profiling inversion of downwelling atmospheric microwave emission, and surface and atmospheric inversion of SMMR and SSM/I brightness-temperature samples.

Dr. Ruf is a member of the IEEE Geoscience and Remote Sensing Society and the American Geophysical Union.

Calvin T. Swift (M'67–SM'69–F'83) was born in Prince William County, VA. He received the S.B. degree from the Massachusetts Institute of Technology in physics in 1959, the M.S. degree from Virginia Polytechnic Institute in physics in 1965, and the Ph.D. degree from the College of William and Mary in 1969.

He was employed as a research engineer by North American Aviation, Downey, CA, from 1959–1962 where he worked on a variety of defense-related problems. In 1962 he was employed by NASA Langley Research Center, Hampton, VA, where he initially conducted research on plasma-covered antennas. After 1970, he was involved in microwave remote sensing of the Earth, and assumed leadership responsibility of a microwave radiometer group at Langley. While at Langley, he held part-time teaching appointments with local universities, and was the organizer of a short course sponsored by the George Washington University. Since 1981, he has been Professor of Electrical and Computer Engineering at the University of Massachusetts, Amherst. He has published in the areas of antennas, wave propagation, plasmas, and microwave remote sensing.

Professor Swift is chairman of U.S. Commission F (Radio and Nonlonized Media) of the International Union of Radio Science (URSI). He served the IEEE Antennas and Propagation Society (AP-S) as Technical Program Chairman of the International AP-S/URSI Symposium held in Williamsburg in 1972, and was twice elected a member of the AP-S Administrative Committee (AdCom); serving as Meetings Chairman, Secretary-Treasurer, Membership Chairman, and Chairman of Long Range Planning. He was twice elected to the Administrative Committee of the IEEE Geoscience and Remote Sensing Society (GRS-S) and was president of the Society in 1985. He was vice chairman of U.S. Commission F of URSI prior to his election to chairman. He has served as a reviewer for many journals and was Guest Editor for the AP-S/JOE (JOURNAL OF OCEANIC ENGINEERING) special joint issue on Radio Oceanography. He is a past Editor of the TRANSACTIONS ON GEOSCIENCE AND REMOTE SENSING and a former Associate Editor of JOE. In 1984, he was awarded a centennial medal from the IEEE.

*

ESTAR prototype.

Alan B. Tanner received the B.S. degree in electrical engineering in 1984 at the University of Massachusetts at Amherst where he is currently enrolled in the Microwave Remote Sensing Laboratory (MIRSL) as a Ph.D. candidate.

He has worked in MIRSL since 1983 and is involved in the development of instrumentation and of data reduction algorithms for remote sensing. Such work has included the deployment of a radiometer on a NOAA aircraft for the sensing of hurricane windspeeds and the development of an

*

David M. Le Vine (M'70–SM'79) received the B.S.E., M.S.E. and Ph.D. degrees in electrical engineering and the M.S. degree in physics from the University of Michigan, Ann Arbor.

He has worked at the Harry Diamond Laboratories, Department of the Army, the Radiation Laboratory, University of Michigan and the Department of Electrical Engineering, University of Maryland. He is currently a member of the Microwave Sensors Branch, Laboratory for Oceans at NASA's Goddard Space Flight Center where his research has focused on the development of techniques for microwave remote sensing of the environment from space.

Dr. Le Vine is a member of the International Scientific Radio Union (URSI) and the American Geophysical Union. He has been elected to Eta Kappa Nu, Tau Beta Pi, and Phi Kappa Phi, was a University of Michigan Fellow and a NASA/ASEE Faculty Fellow, and is the recipient of several service awards from the Goddard Space Flight Center.